# Very high cycle fatigue under tension/torsion loading of mold low alloy steel

Pedro R. da Costa[1], Luis Reis[1], and Manuel Freitas[2]

[1]Universidade de Lisboa Instituto Superior Tecnico
[2]Atlantica Escola Universitaria de Ciencias Empresariais Saude Tecnologias e Engenharia

May 2, 2022

**Abstract**

Ultrasonic fatigue testing is a recent fatigue methodology that applies resonant principles to induce cyclic stresses in a modally designed specimen enabling the application of fatigue damage at very high frequencies. Its primary purpose is to study fatigue life in the Very High Cycle Fatigue regime between 10E07 and 10E09 cycles with a higher performance of time and energy wise compared to conventional servo-hydraulic fatigue testing machines. In this study, an ultrasonic fatigue testing machine was used to carry out multiaxial tension/torsion fatigue tests at a frequency of 20 kHz. The objective was to reach a reliable multiaxial fatigue testing method by modifying only the specimen, with the ability to induce different shear to axial stress ratios. The improved design/methodology of the testing ultrasonic multiaxial method focused first on the innovative design specimens and setup modal behaviour by conducting both numerical and experimental analyses. Laser displacement measurements, thermographic imaging, and rosette strain gauges applied to the specimen's fatigue stress region were carried out to validate the new design concept and compared with the computed results obtained by finite element. A good numerical to experimental results agreement was achieved. A series of fatigue tests were carried out in tension/torsion fatigue to three different combining dimension specimens allowing three different shear/axial stress ratios. The resulting crack initiation angles and fracture surfaces were analysed and compared not only between each other but also with tension-compression and pure torsion ultrasonic tested specimens.

## Very high cycle fatigue under tension/torsion loading of mold low alloy steel

Pedro R. da Costa[1,3], Luís Reis[1,2]and Manuel Freitas[2,3]*

[1]*Instituto Superior Técnico, universidade de Lisboa, Av. Rovisco Pais, 1049-001 Lisbon, Portugal*

[2]*IDMEC, Instituto Superior Técnico, Av. Rovisco Pais, 1049-001 Lisbon, Portugal*

[3]*Atlântica, Instituto Universitário, Fabrica da Pólvora, Barcarena, 2730-036 Barcarena, Portugal*

* Corresponding author: manuel.freitas@tecnico.ulisboa.pt

**Abstract**

Ultrasonic fatigue testing is a recent fatigue methodology that applies resonant principles to induce cyclic stresses in a modally designed specimen enabling the application of fatigue damage at very high frequencies. Its primary purpose is to study fatigue life in the Very High Cycle Fatigue regime between 10E07 and 10E09 cycles with a higher performance of time and energy wise compared to conventional servo-hydraulic fatigue testing machines. In this study, an ultrasonic fatigue testing machine was used to carry out multiaxial tension/torsion fatigue tests at a frequency of 20 kHz. The objective was to reach a reliable multiaxial fatigue testing method by modifying only the specimen, with the ability to induce different shear to axial stress ratios. The improved design/methodology of the testing ultrasonic multiaxial method focused first on

the innovative design specimens and setup modal behaviour by conducting both numerical and experimental analyses. Laser displacement measurements, thermographic imaging, and rosette strain gauges applied to the specimen's fatigue stress region were carried out to validate the new design concept and compared with the computed results obtained by finite element. A good numerical to experimental results agreement was achieved. A series of fatigue tests were carried out in tension/torsion fatigue to three different combining dimension specimens allowing three different shear/axial stress ratios. The resulting crack initiation angles and fracture surfaces were analysed and compared not only between each other but also with tension-compression and pure torsion ultrasonic tested specimens.

**Keywords**

Multiaxial Fatigue; Tension/Torsion; Ultrasonic Fatigue Testing; Very High Cycle Fatigue

## INTRODUCTION

Ultrasonic fatigue testing machines and respective methodologies were created to respond to the need for an energy and time reliable manner of studying fatigue materials behaviour between 10E07 and 10E09 cycles and beyond, which allows the study of the Very High Cycle Fatigue (VHCF) regime [1]. Ultrasonic fatigue testing methods apply resonant principles to achieve very high frequency cyclic stresses. A careful design of the setup, composed of the actuator, amplification components and a specimen, has the objective of using resonance as the means to achieve high enough stress amplitude at a very high frequency.

In order to achieve a working resonance with the desired stress state at the material sample, every present component needs to be modally designed to have cohesive displacement behaviour between each other [2]. In Mason [3] and presently on most utilized ultrasonic tension-compression machines, three different components are designed with their first longitudinal resonant mode (one point of no axial displacement and high-stress amplitude – displacement node): a booster, horn and an hourglass-shaped specimen. Piezoelectric transducers actuators are commonly used to excite the setup in 20 kHz resonance. In this first setup the primary and only objective of the present booster and horn is to amplify the axial cyclic displacement of the resonance inductor axial transducer. The booster is connected to the transducer and also serves as a machine support in its displacement node. The horn is attached to the opposite end of the booster. The hourglass-shape specimen is then attached to the horn other end. The remaining specimen base is denoted the free base and is mainly used for displacement measurements. Also, the specimen is made symmetrical to ensure the highest stress region at the centre, the fatigue testing region. Many different machines have been designed and tested with different testing frequencies, but 1950's Mason [3] 20kHz frequency ultrasonic fatigue machine has become the standardized and most followed method.

Initial ultrasonic fatigue testing machines induced tension-compression to an hourglass-shaped specimen [3]. Additional methodologies with variants surged with different uniaxial and multiaxial stress states: bending [4], biaxial bending [5], pure torsion [6]–[8] and axial-axial cruciform [9]–[11]; fretting [12]; with high and low temperatures [13]; and within a highly corrosive environment [14]. All the referenced ultrasonic fatigue testing machines utilize an axial piezoelectric transducer as the resonance excitation method. Nikitin et al. utilized a rotational piezoelectric transducer to excite a pure torsion stress state in a similar setup as the tension-compression [8]. The use of this different piezoelectric transducer is not common in comparison with the extensive experimental published research on ultrasonic fatigue with axial transducers [15]–[18].

Just as 'conventional' fatigue testing transposed from uniaxial to multiaxial testing mechanisms, Ultrasonic Fatigue Testing (UFT) developments are also following the same trend. The first constructed conventional fatigue machines focused on pure uniaxial cyclical load testing, meaning one cyclical directional load. Multiaxial stresses were later recognised as the leading dynamic stress state in machines and structures [19], meaning two directional loads (biaxial state) or three directional loads (triaxial state). Different examples of multiaxial dynamic loads are present in many industries, including railway, aerospace, industrial manufacturing machines, energy, aerospace, and others [20]–[22].

The present study applies three new different designed specimens to a modification of an ultrasonic fatigue

testing machine capable of inducing a tension/torsion multiaxial stress combination. The created ultrasonic machine applies, just as every previously referenced ultrasonic machine, resonance principles to a given setup of components to reach a 20kHz cyclic multiaxiality in a testing specimen. A detailed explanation of the multiaxial setup followed by the applied specimen geometries is first made, followed by the experimental methodology conducted and the experimental results of fatigue testing.

## ULTRASONIC MULTIAXIAL FATIGUE MACHINE

Vieira et al. [23] designed and tested the first multiaxial tension-torsion ultrasonic setup. The multiaxial machine follows a similar component setup composition to the tension-compression uniaxial method. The machine is composed of an axial piezoelectric transducer, booster, horn and a specimen, in the respective sequence. A special horn design, here denoted multiaxial horn, and a particular triple hourglass-shaped specimen are the present changes that allow to reach the multiaxial tension-torsion stress state.

Like all other ultrasonic machines, all components were designed to have specific resonance modes at the operating 20 kHz frequency. The new designed multiaxial horn has a set of rips that allow transforming the induced cyclic uniaxial displacement from the booster into an axial and rotation displacement combination. Therefore, the horn base where the specimen is connected induces two different in-phase and simultaneous displacements, axial and rotation.

Differently from standard cylindrical fatigue testing geometries, the specimen has three throats. The three reduced cross-section areas allow for a complex resonance excitation in two modes simultaneously, a longitudinal and a rotational mode. As explained, every component needs to be modally designed to have compliant resonant modes with the sequentially attached components. As aforementioned, the multiaxial horn provides both axial and rotational displacement. Therefore, the specimen needs to have a longitudinal mode (just like tension-compression ultrasonic specimens) and a rotational mode at 20 kHz with the highest displacement at the connection region to the horn.

Vieira et al. [23] showed the setup's ability to reach the tension-torsion stress state by using a strain gauge at the specimen fatigue testing region. Unfortunately, the setup was not able to reach full fatigue fracture. Pedro et al. [24] enhance a new design for the multiaxial ultrasonic horn design through finite element analysis (FEA) for higher power settings. Just as Vieira, strain gauges were applied to the tested specimens. From the achieved improvements to the ultrasonic multiaxial setup, the first fatigue fracture was obtained by Costa et al. [25] in steel specimens manufactured directly from a railway wheel. The complete multiaxial setup (booster, multiaxial horn, specimen) is presented in Figure 1 with all present components designations, dimensional specimen variables, throats designations and displacement measuring free base.

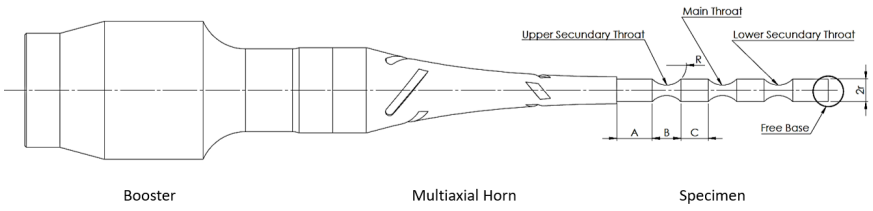


Figure . The complete multiaxial setup (booster, multiaxial horn, specimen) with components designations and respective denotations.

In this study, three different multiaxial specimens were numerically designed through finite element analysis software. The conducted numerical method created and computed was put forwards with the three geometries. The three multiaxial specimens were denoted as Spc $x$and are shown in Figure 2.

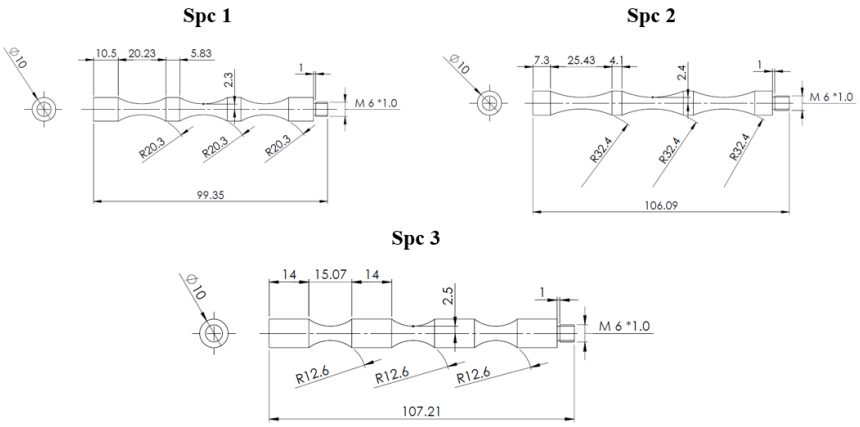


Figure . Three throated tension-torsion tested specimens Spc $x$.

Present study started by computing detailed Finite Element Analysis (FEA) of the specimens and complete setup. From the numerical results, the relation between the displacement (axial and rotational) at the free base to stress (axial and shear) amplitude at the fatigue testing region (Main throat) was obtained together with the specimen and setup displacement and stress distribution. Through it, and taking into account the specimen geometry variables, different shear/axial stress ratios were achieved without changing the multiaxial horn.

## FEA MULTIAXIAL SPECIMEN AND COMPLETE SETUP

Two different FEA were conducted to the three throated specimen, and complete multiaxial setup: free-free no boundary conditions frequency modal analysis, and a steady-state modal analysis with a 1 Newton [N] applied excitation force between 18500 to 21500 Hz. Costa et al. [11] conducted a similar numerical methodology to the ultrasonic cruciform specimens and respective ultrasonic booster horn setups.

The computed FEA were divided into two subchapters, the specimen alone followed by the complete multiaxial setup. Significant conclusions and data were taken to be compared to the experimental results.

Multiaxial specimen

Initial specimen design by Vieira et al. [23] had specific geometry variables relations associated with the rotational displacement. The initial basic knowledge of how the rotational resonance was associated with the specimen geometry limited the creation of combinations that allowed for the required 20 kHz on both the longitudinal and rotational modes. Costa et al. [25] showed from a detailed numerical study on the resulting modal shape, that Vieira's specimen geometry presented similar shear stress amplitude in the three throats. Such shear stress distribution was associated with the displacement to dimension relation, which resulted in equal rotation displacement in all sections. By reducing the cylindrical section between throats the same deformation energy would be more concentrated, resulting in higher rotation. Higher rotation in the cylindrical sections between throats will not only result in higher shear stress amplitude in the main throat, but it will also result in a different shear stress amplitude for the same rotation displacement excitation from the multiaxial horn. Therefore, by altering the specimen dimensional combination relations, different shear/axial ratios can be obtained without the need for a different multiaxial ultrasonic fatigue setup.

The three different tension/torsion specimen geometries (Figure 2) were analysed by FEA with the different dimensional combinations. Figure 3 presents the resulting normalized displacement and stress distribution of Spc2 geometry with a 0.77 shear/axial stress ratio.

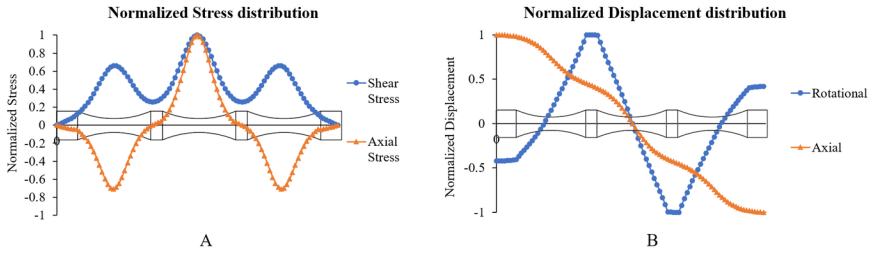


Figure . Spc normalized displacement and stress distribution

A clear difference in shear stress amplitude between the secondary and the main throat is visible in Figure 3. This difference will also prevent one present issue when testing Vieira's specimen. Due to the complex behaviour of the rotational mode an increase in shear stress on one of the secondary throats was present in some specimens. This was observed by thermal control during ultrasonic excitation, where a secondary throat would present higher or equal heat generation to the Main throat. Meaning, some specimens presented higher stress amplitude outside the intended fatigue testing region. An undesirable behaviour that made the ultrasonic multiaxial method unable to reach a quantifiable and the intended fatigue failure.

Multiaxial tension-torsion ultrasonic setup

Having achieved 20 kHz first longitudinal and 20 kHz third rotational modes in three different geometries with different shear/axial stress ratios, the specimens were attached to the booster and multiaxial horn setup. Both the free-free frequency modal and steady-state modal FEA were computed. For the steady-state FEA the 1N force was applied to the booster as to replicate the axial transducer excitation.

An example of the displacement (axial and rotational) and stress (axial and shear) distributions of the booster multiaxial horn and three throated specimen is shown in Figure 4.

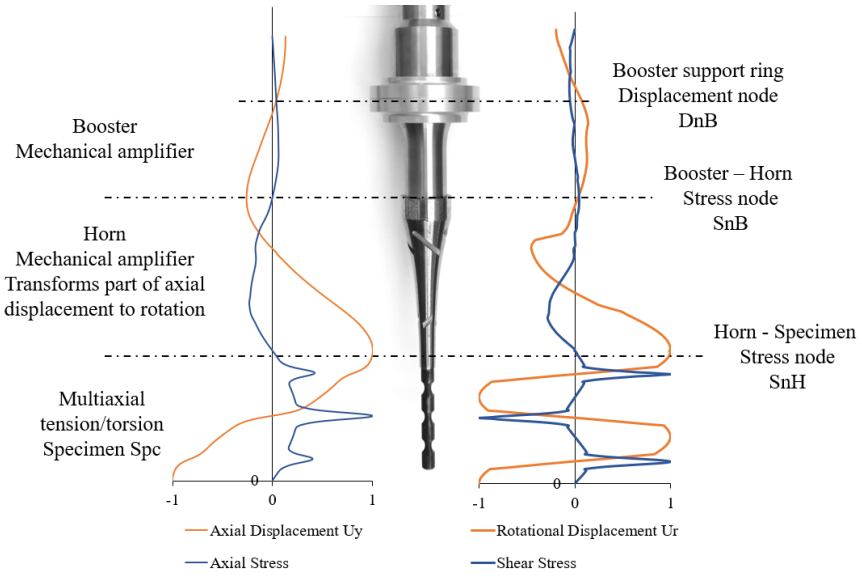


Figure . Multiaxial ultrasonic complete setup displacement and stress distribution.

Figure 4 does not replicate the increased shear stress amplitude to the secondary throats observed in Spc3 of Figure 3. There are significant details to be discussed in Figure 4 resulting distributions. When designing the full ultrasonic multiaxial setup the rotation distribution was made so that the rotation induced to the axial

transducer was as low in amplitude as possible, because this equipment was not prepared to have torsional load. Therefore, to safeguard the axial piezoelectric transducer, the resulting rotation was made as low as possible.

Between every component, from the transducer to the specimen, there must be a present stress node (high displacement, low-stress region). If there is deformation between connections, the excited resonance could affect the correct contact, detach when in operation and even generate heat due to friction. The resulting behaviour could eventually alter or damage the setup, and the resulting induced cyclic stress to the specimen making the fatigue test no longer be valid.

The present ultrasonic multiaxial setup showed the correct positioning of the stress nodes at the component's contact region. Following the FEA steady-state analysis, one Newton excitation was carried out across the frequencies between 18500 and 21500 Hz of the complete setup and all three Spc x specimens showed to be correctly excited in the prescribed resonant mode. The steady-state computed Spc2 displacement (at the free base) and stress amplitude (at the fatigue testing region) across the frequency range (18500 Hz to 21500 Hz) is presented in Figure 5. Three different instances where there is a present resonant response of the setup and are identified in Figure 5. The 20 kHz Mode of Interest (MI), the one to be excited by the axial transducer and two other non-desirable resonant modes denoted Parasite Modes (PM).

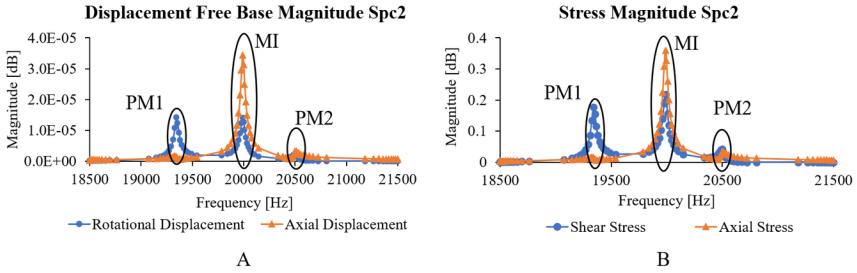


Figure 5. FEA steady-state multiaxial ultrasonic setup with Spc2 displacement at the free base and stress amplitude at the fatigue testing region across 18500 to 21500 Hz.

When studying ultrasonic cruciform specimens, Costa et al. [11] also observed parasite resonant modes that were close in frequency proximity to the resonant mode of interest. Experimental measurements showed that one parasite mode was altering the specimen's desirable resonant mode shape response.

Figure 5 identified PM2 does not show significant displacement or stress amplitude because it is a torsional mode with low axial displacement. Since its mode shape is not cohesive with the excitation method, there will not be a significant displacement/deformations associated with PM2. On the other hand, PM1 has significant stress and displacement amplitude with coherent displacements to the transducer excitation and the MI. Following Costa et al. [11] conclusions, PM1 will have an effect on the final resonant mode shape of the specimens, and therefore, it will affect the final stress ratio result. The experimental results indeed proved this conclusion.

## EXPERIMENTAL METHODOLOGY

The material chosen for the experimental test is an AISI P20 low alloy mold steel. Tensile, hardness and metallurgical analyses were conducted. The main material properties and chemical composition are presented in table 1.

Table . AISI P20 medium carbon steel chemical composition and mechanical properties.

**Chemical Composition [mass%]**

| Fe | Mn | Cr | Ni | Mo |
|---|---|---|---|---|

| | | | | |
|---|---|---|---|---|
| 95 | 1.39 | 1.88 | 1.01 | 0.17 |
| **Mechanical Properties** | **Mechanical Properties** | **Mechanical Properties** | **Mechanical Properties** | **Mechani** |
| E, Young Modulus [GPa] | E, Young Modulus [GPa] | Yield Stress [MPa] | Yield Stress [MPa] | Ultimate S |
| 203 ±2 | 203 ±2 | 923 ±5 | 923 ±5 | 1040 ±4 |

From Table 1 mechanical properties, together with the material's density, the three different Spc multiaxial specimen geometries possible that were numerically designed, were manufactured and afterwards tested.

For every manufactured specimen, a frequency analysis was conducted, followed by a thermal scan. Rosette strain gauges were applied to the main throat region in all specimens, i. e. all specimens with reached 20kHz resonance and higher heat generation at the main throat. Simultaneously, both the longitudinal and rotational displacements were also measured in the free base of the specimen. The same method applied by Vieira et al. was followed for measuring the rotation where two notches were machined in the specimen's free base. Figure 6 presents the multiaxial testing setup and the machined grooves for rotation measurement. Strain and displacement measurements were carried out to several power settings with the multiaxial horn and also with two different uniaxial tension-compression horns.

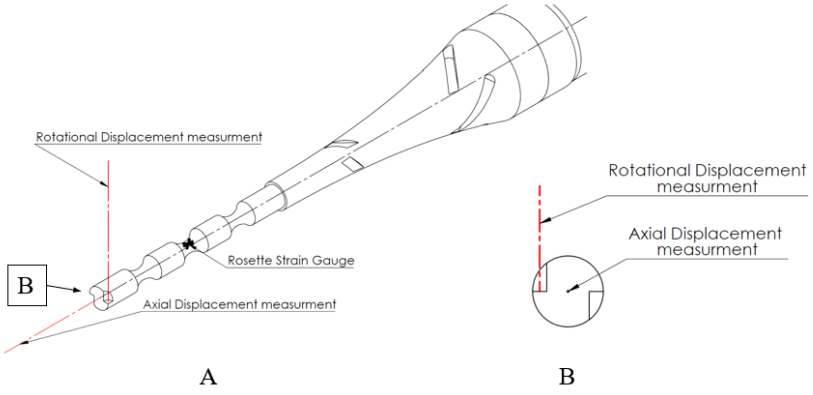


Figure . (A) Ultrasonic multiaxial laser and strain gauge experimental setup; (B) Free base laser placement with machined groves representation for rotational measurement.

## RESULTS AND DISCUSSION

The specimens with the geometries presented in Figure 2, by having considerably higher shear stress at the main throat, the stress combination difference between secondary and main throats resulted in a noticeable heat generation difference. All but one specimen presented considerably higher heat generation at the main throat through thermal imaging, Figure 7. Such a single specimen showed to be excited on its PM1. As expected, since in the PM1 the multiaxial specimen horn connection is no longer a stress node, a friction heat generation is present that exceeds the heat generated by the throats. A correct thermal behaviour specimen and the Spc 2 PM1 excited specimen under thermal imaging are shown in figure 7.


Figure . Multiaxial ultrasonic specimens under thermal imaging: (A) correctly working MI specimen; (B) PM1 Spc2 specimen.

An experimental frequency analysis of the setup showed all specimens could be resonance excited. It also showed the excitation of the second mentioned mode in some specimens, the numerically determined PM1. The laser measurements with both constant frequency displacement and frequency analysis proved the PM1 presence and the resulting effect on the specimen rotational displacement. The mode is easily identified by the higher base rotation and a displacement phase change. All specimens with a close PM1 frequency also exhibited a noticeably high heat generation at the secondary lower throat. This is consistent with a close frequency mode observed in FEA. Figure 8 shows the laser output of the conducted frequency analysis of a Spc2 specimen, where the PM1 presence with a lower frequency is easily observed. As also predicted by FEA, there was no observable displacement amplitude associated with the PM2.

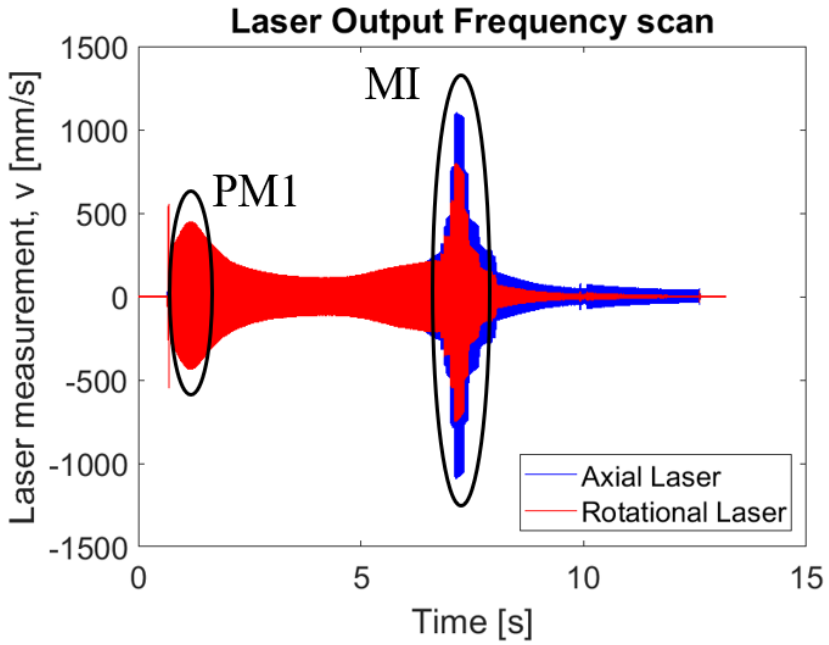


Figure . Axial and rotational laser output of an Spc2 specimen in the multiaxial ultrasonic setup under frequency response analysis.

The axial modal shape proved to be very stable and replicated between all specimens for the same geometry. The steady-state analysis presented a low difference from the obtained experimental trend across all

conducted measurements. Figure 9 shows Spc1 to Spc3 experimental and FEA axial displacement to axial stress results.

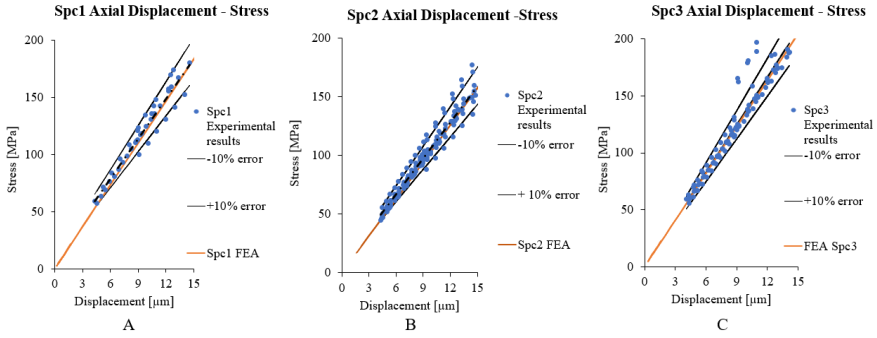


Figure . Comparison between experimental and numerical axial displacement at the free base to axial stress amplitude at the fatigue testing region.

Most axial displacement stress experimental results between all specimens follow the same linear trend with a good agreement with the FEA calculated. Only a few exceptions have exceeded a 10% difference. The negligible difference in all three specimens between the determined experimental mean and the numerical steady-state modal analysis proves the ability of the computed FEA method as a tool to determine the three throated specimens axial stress through the experimentally measured free base axial displacement.

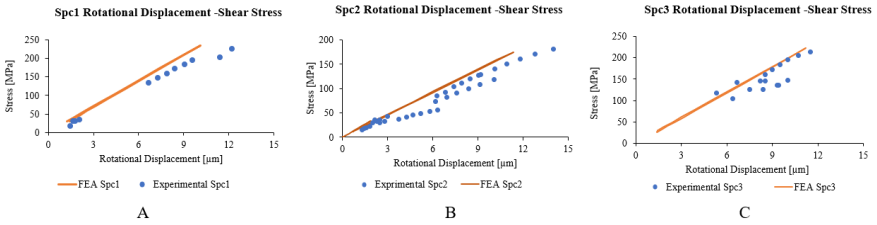


Figure . Comparison between experimental and numerical rotational displacement at the free base to shear stress amplitude at the fatigue testing region.

The same analysis was conducted on all three geometries regarding the rotation displacement to shear stress ratio and is shown in Figure 10. A considerable difference is present between results calculated by FEA and experimental results in some specimens. Shear stress values tend to be lower than predicted by FEA. Therefore the resulting shear to axial stress ratio variation between specimens is again associated with PM1 influence and the specimen high geometrical sensitivity. PM1 influence leads to a changing rotation displacement to shear stress relation. Still, some measured points presented a good linear agreement with FEA, as shown in Figure 10.

The resulting axial and shear displacements and respective experimental strain measurements show a variation in shear amplitude between specimens but a constant displacement to tension-compression between each specimen geometry. The axial displacement and resulting deformation present a more stable response since its setup distribution has fewer displacement and stress nodes, and it is the dominant displacement provided by the transducer. The rotation resonance has more rigidity dependent regions and considerably more displacement and stress nodes, resulting in a higher sensibility to variation between specimens and affecting neighbour resonant modes.

Fatigue life

Having determined the shear and axial induced stress amplitudes for different transducer settings, the shear/axial stress ratios and the resulting displacements at the free base, several specimens were subjected to a constant stress amplitude at R=-1 stress ratio until fatigue failure.

Figure 11 shows a Stress to Number of cycles S-N curve where the strain gauge measured axial stress is plotted against the resulting fatigue life for different Shear/Axial Stress Ratio (sasr). Since the axial stress is much more stable than the shear stress within the same specimen geometry, the axial stress was first associated to the number of cycles to failure. Certainly, an influence of the shear stress is present, therefore, the "sasr" measured values where divided into higher and lower than Von Mises 0.577 equivalent stress ratio, respectively, higher than 0.577 'sars' specimens that present higher shear than axial stress, while lower than 0.577 the axial stress is the predominant. They present different behaviour concerning fatigue life, as expected and these results are comparable with classic tension/torsion fatigue tests carried out on classical servo-hydraulic machines.

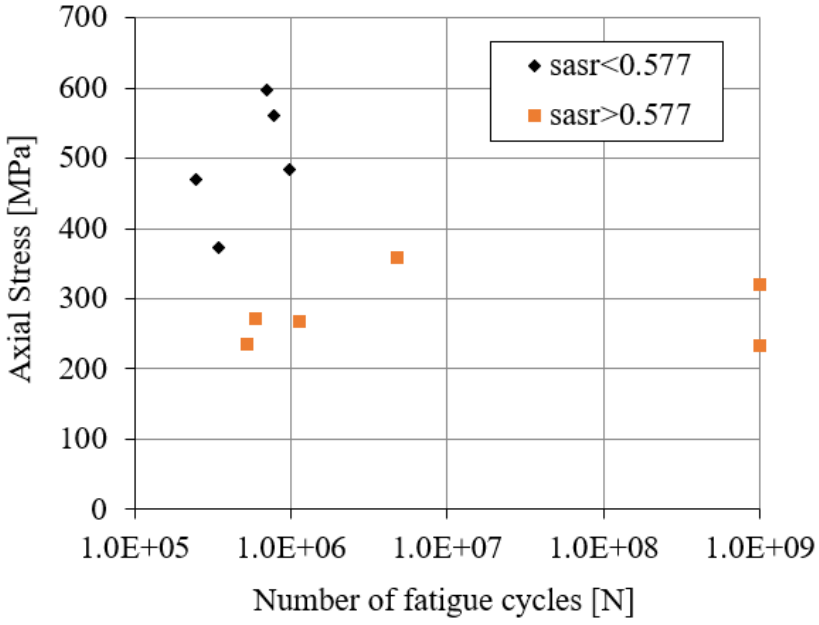


Figure 11. Measured axial stress to fatigue life cycles for different shear to axial stress ratio ('sasr')

Results presented in Figure 11 show a high scatter on fatigue life for identical induced axial stresses. Some scatter is always associated with fatigue results, but in this study the higher scatter observed is also associated, not only to multiaxial fatigue tests where shear and axial stresses are applied, but also to the variability of the shear to axial stress ratio. This variability is associated with small length differences between throats, which cause some proximity to torsional Parasite Modes, as already mentioned before.

The influence of shear to axial stress ratio is also shown in Figure 12, which shows the influence of "sasr" on multiaxial (tension/torsion) fatigue life. It is also clear the influence of the shear stress and of the shear to axial stress ratio on multiaxial fatigue.

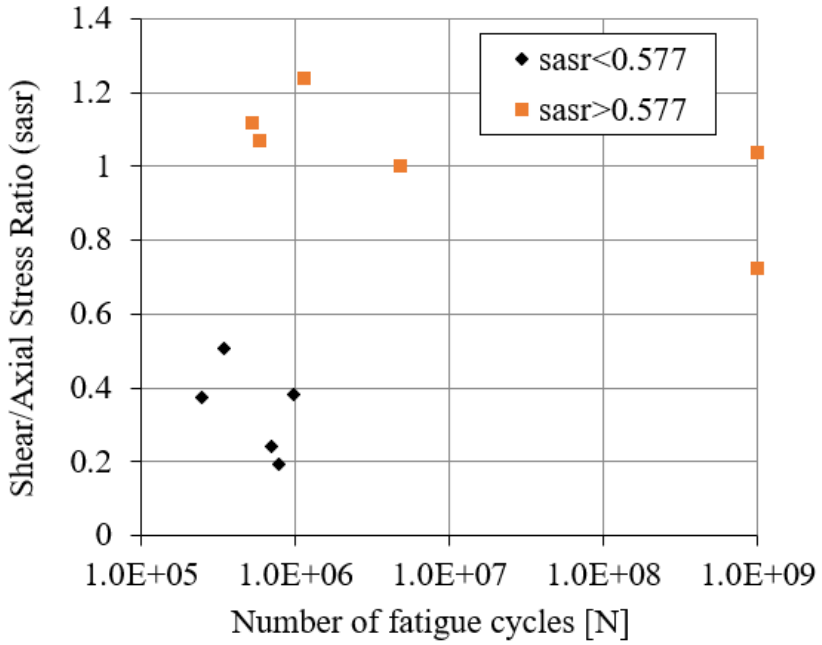


Figure 12. Shear to axial stress ratio to number of fatigue cycles

An unclear HCF and VHCF stress life was achieved which results in some scatter. This different stress combinations between shear and axial stress did not allow for higher stresses or lower life fatigue results. The non-fully present VHCF behaviour is associated with the lower strength and hardness of steel here tested. As the hardness and general strength increase, the VHCF regime failure appears and becomes more pronounced [26]. The research led by Aiguo Zhao et al. [27] used the same material with different heat treatments. As the material has a higher annealed temperature, a more ferritic microstructure is obtained with a corresponding lower ultimate stress, Vicker's hardness and lower fatigue stress-life strength. When comparing all four different microstructures, from lower strength ferritic to higher strength martensitic microstructures, the results showed failure in a higher number of cycles and crack initiation transition from surface to internal regions.

**Fractographic analysis**

The specimens were fully fractured in servo-hydraulic machines after reaching resonance loss due to the nucleated fatigue crack. All fractured surfaces were first analysed at their crack initiation location and angle. Since all specimens presented a surface crack initiation, a simple microscope view was used with image analysing software to determine the initiation angle. Figure 13 shows one example of a specimen tested at a shear/axial stress ratio 0.37 under a microscope for crack initiation angle determination.

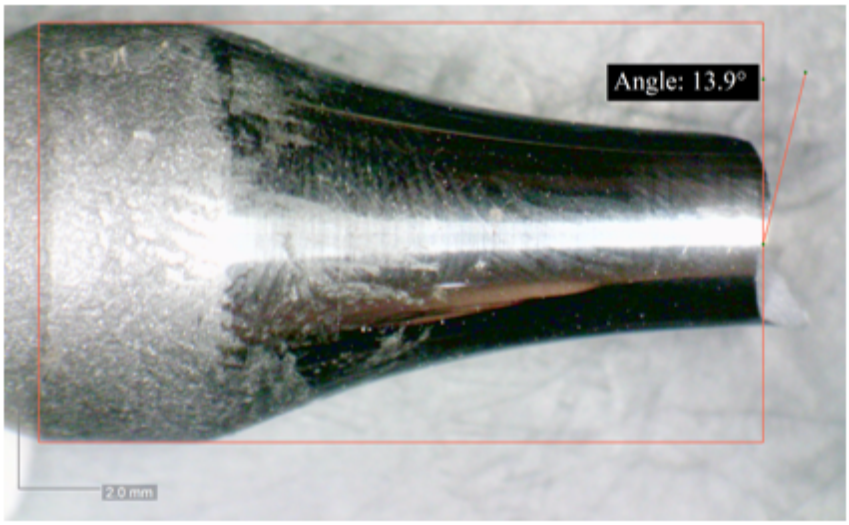


Figure 13. Surface crack initiation angle measurement.

The crack initiation angle showed an increasing tendency as the shear/axial 'sasr' ratio increased, thus having a clear influence of shear on the crack initiation angle. All fatigue fracture crack initiation angles were associated with the respective induced 'sars' in Figure 14, showing the increasing tendency. As the present 'sasr' exceeds the Mises 0.577 ratio the cack initiation ratio tends towards the $45^{o}$ crack initiation, therefore showing the dominant shear influence offer the fatigue induced crack and propagation.

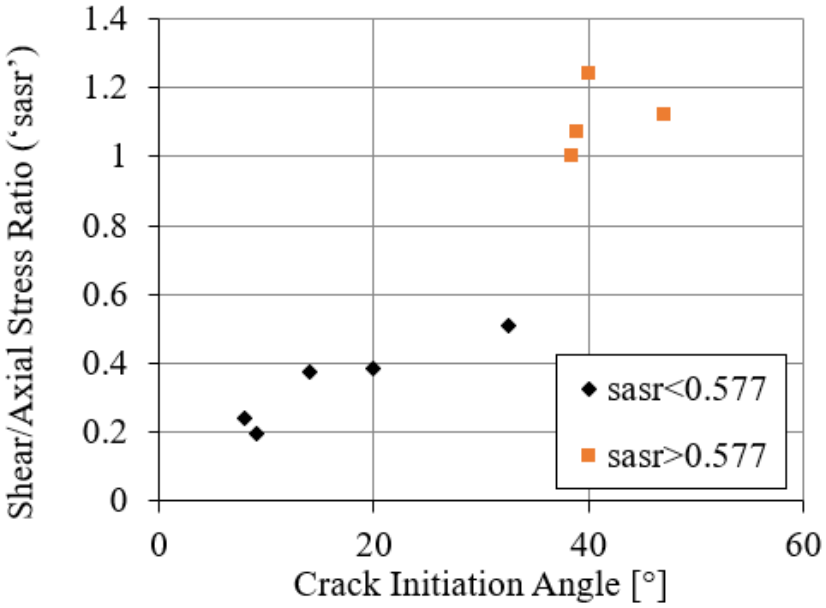


Figure . Crack initiation angle to shear/axial stress ratio.

As predicted, distinct mixed-mode crack propagation is present in all specimens. The fatigue crack surface indicates a mixed-mode I and II crack propagation. With the increase in shear/axial stress ratio, more

predominant shear damage marks were present. In the mean and high-stress ratio specimens, the crack propagation has an initial stage with a 'smoother' surface, followed by the appearance and increasingly more prominent radial marks. Figure 15 shows the two described regions and the presence of radial marks in detail for a specimen with a 0.51 shear to axial stress ratio specimen.

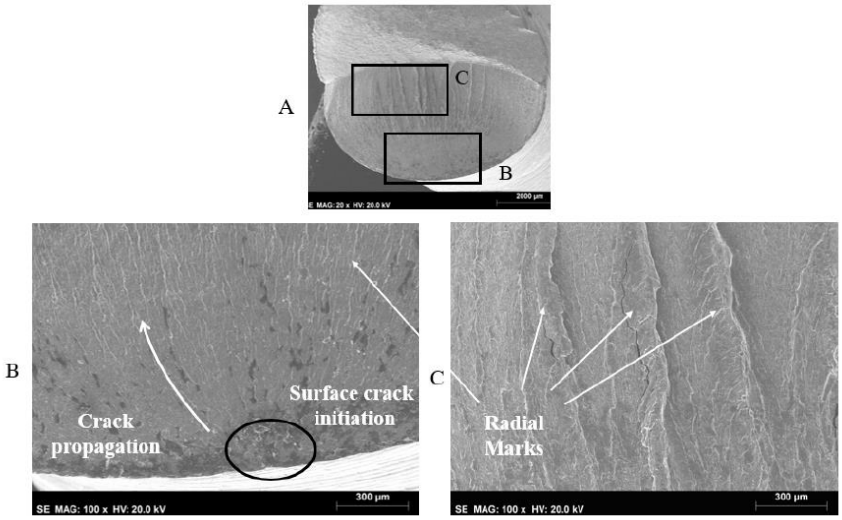


Figure 15. Fatigue fracture surface of a multiaxial specimen with a 0.51 shear/axial stress ratio.

The radial marks are associated with high shear deformation. Pure torsional specimens have shown similar radial marks propagation zones [8] and they are indeed much more pronounced with higher shear stress amplitude multiaxial specimens. The radial marks increased in size from crack initiation to final fracture, indicating increasingly dominant shear damage across the fatigue crack propagation. Therefore, the fatigue crack propagates as a mixed-mode I and II with the increasing dominance of mode II.

Figure 16 compares the fatigue crack surface of an axial tension-compression and two tension/torsion specimens tested in ultrasonic fatigue testing machines.

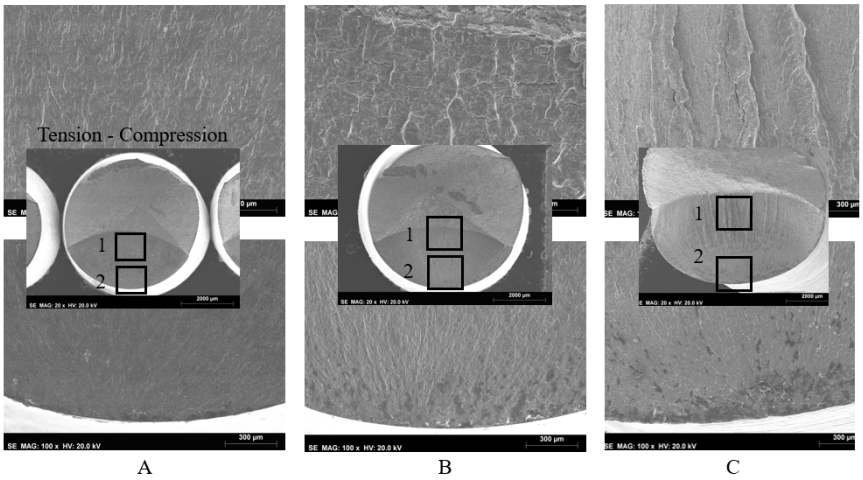


Figure 16. Fatigue fracture surface comparison between ultrasonic fatigue (A) Tension-compression; (B)

multiaxial 0.37 shear/axial ratio; (C) multiaxial 0.51 shear/axial ratio.

From the observation of the surface fracture, there is a transformation from tension-compression associated intricacies to pure torsion of low to high shear/axial stress ratio multiaxial specimens. The lowest 0.37 stress ratio specimen (Figure 16.B) does not fully show the identified initial smooth surface to radial marks propagation regions in figure 15. Its dominant axial stress resulted in a dominant crack mode I propagation which shows a similar crack surface to tension-compression specimens with only minor shear radial marks very close to the final fracture. With a higher shear/axial stress ratio, the initial smooth surface region appears, there will be a higher crack initiation and propagation angle tendency, and there will be increasingly higher and more pronounced radial marks.

## CONCLUSIONS

Through FEA analysis, multiaxial tension/torsion specimens' geometries were achieved. The specimen geometry was manipulated to reach different shear stress amplitudes for the same induced rotation of resonance excitation. Also, a higher stress combination amplitude was reached in the fatigue testing region, maintaining no present deformation at the multiaxial horn-specimen connection.

Three different geometries were designed and machined following the resulting FEA study. The new specimens proved more reliable by guarantying the highest stress amplitude in the main throat, and therefore, only the region of interest reached the intended shear/axial stress combination.

All obtained fracture surfaces proved fatigue crack propagation associated with shear and axial cyclic stresses. By comparing different shear/axial stress ratio specimens, a clear trend in crack propagation details as initiation and propagation angle and shear damage radial marks increased with the increase of the induced ratio. Therefore, all applied specimens were subjected to the intended and measured multiaxial fatigue until the end of every conducted ultrasonic fatigue test

## ACKNOWLEDGMENTS

This work was supported by FCT, through IDMEC, under LAETA, project UIDB/50022/2020. Financial support from Portuguese Fundação para a Ciência e Tecnologia (FCT) is acknowledged through project PTDC/EMS/PRO/5760/2014. The authors also acknowledge the provided support by FCT for the main author PhD scholarship 2020.06550.BD.

## REFERENCES

[1] C. Bathias, *Fatigue Fract. Eng. Mater. Struct.* , 1999, vol. 22, pp. 559–565.

[2] M. Freitas, V. Anes, and D. Montalvao, *An. Mecânica la Fract.* , 2011, vol. 1, no. 28, pp. 335–340, [Online]. Available: http://uhra.herts.ac.uk/ha.

[3] C. Bathias and P. C. Paris, *Gigacycle fatigue in mechanical practice* . 2005.

[4] H. Q. Xue, H. Tao, F. Montembault, Q. Y. Wang, and C. Bathias,*Int. J. Fatigue* , 2007, vol. 29, pp. 2085–2093.

[5] C. Brugger, T. Palin-Luc, P. Osmond, and M. Blanc,*Procedia Struct. Integr.* , 2016, vol. 2, pp. 1179–1180.

[6] I. Marines-Garcia, J. P. Doucet, and C. Bathias, *Int. J. Fatigue* , 2007, vol. 29, no. 9–11, pp. 2094–2101.

[7] H. Q. Xue, E. Bayraktar, I. Marines-garcia, and C. Bathias,*Manuf. Eng.* , 2008, vol. 31, no. 2, pp. 391–397, [Online]. Available: http://www.journalamme.org/papers_vol31_2/31233.pdf.

[8] A. Nikitin, C. Bathias, and T. Palin-Luc, *Fatigue Fract. Eng. Mater. Struct.* , 2015, vol. 38, no. 11, pp. 1294–1304.

[9] P. R. da Costa, D. Montalvão, M. Freitas, R. Baxter, and L. Reis, *Fatigue Fract. Eng. Mater. Struct.* , 2019, vol. 42, no. 11, pp. 2496–2508.

[10] D. Montalvão, A. Blaskovics, P. R. da Costa, L. Reis, and M. Freitas, *Int. J. Comput. Methods Exp. Meas.* , 2019, vol. 7, no. 4, pp. 327–339.

[11] P. R. da Costa, L. Reis, D. Montalvão, and M. Freitas,*Int. J. Fatigue* , 2021, vol. 152, no. June.

[12] Z. D. Sun, C. Bathias, and G. Baudry, *Int. J. Fatigue* , 2001, vol. 23, no. 5, pp. 449–453.

[13] C. Bathias, *Int. J. Fatigue* , 2006, vol. 28, no. 11, pp. 1438–1445.

[14] R. Pérez-Mora, T. Palin-Luc, C. Bathias, and P. C. Paris,*Int. J. Fatigue* , 2015, vol. 74, pp. 156–165.

[15] H. Mayer, *Fatigue and Fracture of Engineering Materials and Structures* , vol. 39, no. 1. Blackwell Publishing Ltd, pp. 3–29, Jan. 01, 2016.

[16] T. SAKAI, *J. Solid Mech. Mater. Eng.* , 2009, vol. 3, no. 3, pp. 425–439.

[17] A. Tridello, *Metals (Basel).* , 2019, vol. 9, no. 133.

[18] P. R. da Costa, M. Sardinha, L. Reis, M. Freitas, and M. Fonte,*Forces Mech.* , 2021, vol. 4, no. May, p. 100024.

[19] M. de Freitas, *Theor. Appl. Fract. Mech.* , 2017, vol. 92, pp. 360–372.

[20] L. Reis, B. Li, and M. De Freitas, *Int. J. Fatigue* , 2014, vol. 67, pp. 191–202.

[21] V. Bonnand, J. L. Chaboche, P. Gomez, P. Kanouté, and D. Pacou,*Int. J. Fatigue* , 2011, vol. 33, no. 8, pp. 1006–1016.

[22] P. Costa *et al.* , *Machines* , 2020, vol. 8, no. 2.

[23] M. Vieira, L. Reis, M. Freitas, and A. Ribeiro, *Theor. Appl. Fract. Mech.* , 2016, vol. 85, pp. 2–8.

[24] P. Costa, M. Vieira, L. Reis, A. Ribeiro, and M. de Freitas,*Int. J. Fatigue* , 2017, vol. 103, pp. 248–257.

[25] P. R. da Costa, H. Soares, L. Reis, and M. Freitas, *Int. J. Fatigue* , 2020, vol. 136, no. March, p. 105581.

[26] Y. Murakami, T. Nomoto, and T. Ueda, *Fatigue Fract. Eng. Mater. Struct.* , 1999, vol. 22, no. 7, pp. 581–590.

[27] A. Zhao, J. Xie, C. Sun, Z. Lei, and Y. Hong, *Int. J. Fatigue* , 2012.